Propagation Parameter Estimation, Modeling and Measurements for Ultrawideband MIMO Radar

Jussi Salmi, *Member, IEEE*, and Andreas F. Molisch, *Fellow, IEEE*

***Abstract*—Ultrawideband (UWB) radar is a promising method for reliable remote monitoring of vital signs. The use of multiple antennas at transmitter and receiver (MIMO) allows not only improved reliability, but also better accuracy in localization and tracking of humans and their various types of movement. This paper describes an experimental demonstration of localizing a test subject and tracking his breathing under ideal conditions. The UWB MIMO channel, which includes the test subject as well as other objects, is modeled as a superposition of multipath components (MPCs). From the measured data one can extract the parameters of the MPCs, including their directions and delays, which allows localization of the test subject as well as tracking the breathing motion. Since the breathing pattern of the test subject induces delay variations of the diaphragm-reflected MPC that are much smaller than the Fourier resolution limits, the high-resolution RIMAX algorithm (iterative maximum-likelihood estimation scheme) is employed together with a path detection scheme for determining and tracking the MPC parameters. Furthermore, it is illustrated that with a wideband array model, the requirements for antenna spacing are not as limited as for conventional narrowband array processing. Through controlled experiments with a vector network analyzer and a virtual antenna array observing both an artificial "breathing" object as well as a human subject, it is shown that one can accurately estimate the small scale movement from human respiratory activity. This is achieved both for line-of-sight between transmitter, receiver, and objects, as well as for non-line-of sight.**

***Index Terms*—array signal processing, multipath channels, position measurement, propagation measurements, parameter estimation, ultrawideband antennas, ultrawideband radar, virtual antenna array**

I. Introduction

As life expectancy increases, the range of diseases that can be treated expands and tasks like care of the elderly are becoming increasingly important. While medical advancements have dramatically improved the quality of care, the cost of providing care has also significantly increased. Dramatic reduction in costs can be achieved by exploiting information technology, new sensing mechanisms, and automated data collection. A particularly promising area is the continuous or quasi-continuous sensing of vital health signs, i.e., parameters that are indicative of a person's health, such as breathing activity.

Part of this work was presented at Asilomar Conference on Signals, Systems, and Computers 2010. The research was partially funded by Academy of Finland. The first author would like to thank Finnish Technology Promotion Foundation (TES), and Walter Ahlström foundation for financial support.

J. Salmi was, and A. F. Molisch is with Department Electrical Engineering, University of Southern California, Los Angeles, CA (e-mail: {lastname}@usc.edu). J. Salmi is currently with Aalto University School of Electrical Engineering, SMARAD CoE, Espoo, Finland (e-mail: {firstname.lastname}@aalto.fi).

While body-mounted sensors can provide these data with great reliability, there are many situations where the inconvenience of having to constantly wear such sensors renders it impractical. Therefore, remote monitoring is highly desirable. Various methods for remote breathing monitoring have been studied at least since 1975, when [1] demonstrated the observation of phase shifts of microwave chirp signals reflected off the chest of a rabbit. Relatively narrowband Doppler radars (see, e.g., [2], [3] and references therein) are by far the most popular method, as they require relatively small hardware effort. However, their drawback is that they do not allow the localization of the target; this also leads to increased difficulty in separating multiple breathing objects and suppressing interference. Further improvement can be achieved by using multiple antenna elements at transmitter and/or receiver. For the conventional Doppler radar case, [4] and [5] demonstrated the ability to resolve multiple sources.

Further performance improvements can be achieved by ultrawideband (UWB) radar. UWB provides high delay resolution, and thus has the ability to determine the range to either active or passive reflectors with high accuracy [6], [7]. This allows to more accurately localize the breathing subject [8] and track the small movements of the diaphragm during breathing. A number of recent papers have provided system designs and/or experimental results, such as [9]–[12]. These papers use a single transmit and single receive antenna, usually a horn antenna that is pointed towards the target. This is useful in controlled scenarios where the location of the test subject is known.

In this paper we investigate a scenario were the location of the subject is not predetermined, but finding it is one of the goals of the measurement. This can be achieved by combining UWB signalling (providing high range resolution) with the directional resolution capability of multiple antenna elements. The underlying theoretical framework formulates a wideband antenna array model and employs the double-directional radio propagation channel model [13] to characterize the UWB channel as a superposition of plane waves (multipath components, MPCs). The characteristics of the MPCs form the basis for the subject localization and the tracking of the breathing. We first establish the model in a general form, applicable to arbitrary antenna array configurations and supporting also polarization aspects. We then give an example of a reduced model, applicable to the employed measurement setup. The paper also discusses modeling of wideband antenna arrays, along with a description of a virtual array model. The virtual array is similar to synthetic aperture radar (SAR), employed recently in through-the-wall imaging, see e.g. [14], [15]. However, the virtual array differs from SAR imaging by relying on

the MPC model, which describes the radio channel as plane waves observed at a single point in space, namely the array phase center. This also limits the total size of the array, as the MPC should originate in the far field of the array.

The processing of the measurement data requires the decomposition of the observed channel response into a superposition of MPCs. For this purpose, we formulate a Maximum Likelihood (ML) based path detection framework, and jointly estimate the MPCs using a modification of the RIMAX [16] algorithm. This approach allows to overcome the Fourier limit of the delay resolution, which in our case is about 5 cm and thus insufficient for identification of the movement from breathing.

The multi-antenna, UWB impulse responses are measured by a vector network analyzer (VNA) combined with a virtual antenna array. This approach does not provide real-time capabilities, and would have to be replaced by a faster excitation combined with real or switched antenna arrays for an actual deployment. However, it is eminently suitable for a proof-of-concept, and shows advantages due to better calibration of the underlying signals. For the same reason, this approach for measuring MIMO-UWB channels is in general use for channel sounding [17], although real-time implementations exist as well [18]. We show experimental results, both line-of-sight (LOS) and non-line-of-sight (NLOS), from anechoic chamber measurement for detecting small scale ($\pm$ 15 mm) movement of both a passive, artificial target, as well as a human holding his breath with empty and full lungs, respectively. This information, together with the estimates of the absolute delays and angles of the corresponding MPCs, can be further utilized for passive localization and surveillance of humans or animals. Part of this work was presented in [19], where the discussion was limited to LOS measurement of an artificial object.

The paper is structured as follows. Section II introduces the system model, including virtual antenna array model and the double directional MPC model. Section III describes the experiments conducted in an anechoic chamber. Section IV introduces the parameter estimation framework, that is applicable to the performed measurements. Section V illustrates the results from the measurements and concluding remarks are given in Section VI.

The following notational conventions are used throughout the paper.

- Boldface upper case letters (Roman $\mathbf{A}$ or Greek $\mathbf{\Sigma}$) denote matrices and lower case ($\mathbf{a}$, $\boldsymbol{\sigma}$) denote column vectors. Calligraphic uppercase letters ($\mathcal{A}$) denote higher dimensional tensors.
- The vector $\mathbf{a}_i = (\mathbf{A})_i$ denotes the i^{th} column of a matrix $\mathbf{A}$ and the scalar $a_j = (\mathbf{a})_j$ denotes the j^{th} element of a vector $\mathbf{a}$.
- Non-boldface upper case letters (N) denote constants, and lower case (a) denote scalar variables.
- Superscripts $^{\text{T}}$, and $^{\text{H}}$ denote matrix transpose, and Hermitian (complex conjugate) transpose, respectively.
- Operator $\diamondsuit$ denotes Khatri-Rao (column-wise Kronecker) product.
- Symbol $\hat{\boldsymbol{\theta}}$ denotes an estimate of the vector $\boldsymbol{\theta}$.
- Operation $\text{vec}\,(\bullet)$ stacks all the elements of the input tensor into a column vector.
- Operation $\underset{M_1 \times \cdots \times M_N}{\text{reshape}}\,(\bullet)$ transforms a given entity, typically a vector, into an N-dimensional tensor, see also [20].
- Operation $\underset{[j_1 \ \cdots \ j_N]}{\text{permute}}(\bullet)$ permutes the order of tensor dimensions, e.g., $\underset{[2\ 1]}{\text{permute}}(\mathbf{A}) = \mathbf{A}^{\text{T}}$, see also [20].

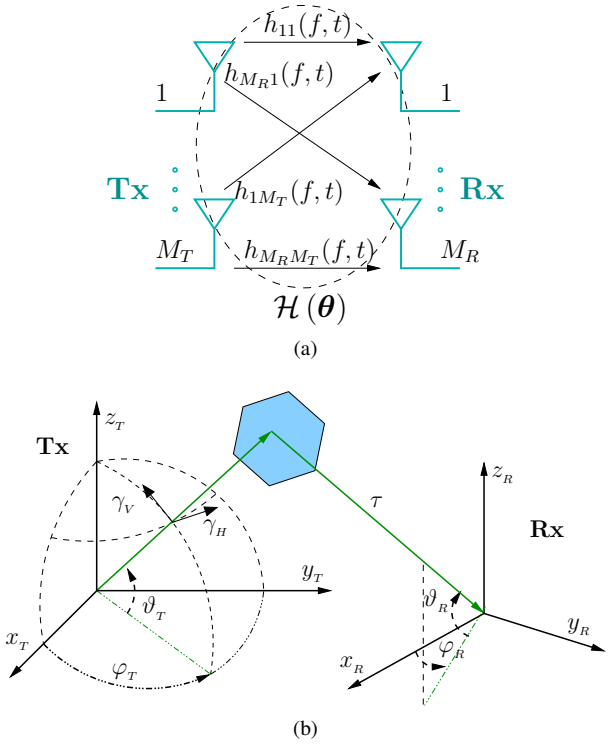

Fig. 1: MIMO channel modeling concept. (a) The channel tensor $\mathcal{H}(\boldsymbol{\theta})$ is defined as the transfer function between all the Tx/Rx antenna port pairs. (b) The parameters of the double directional propagation path model are defined w.r.t. two points in space, namely the array phase centers.

II. System Model

The considered system is based on measuring and characterizing the UWB radio propagation channel between two antenna arrays, one transmitting (Tx, T) and the other receiving (Rx, R). Measurements provide the transfer function between all Tx/Rx antenna port pairs, as illustrated in Figure 1a. However, the double-directional propagation channel model, illustrated in Figure 1b, is defined between two points in space, namely the array phase centers. Hence, the complete channel model is comprised of two main components: i) The mapping of the MPCs onto the antenna ports, i.e., the antenna array model, and ii) the double-directional radio wave propagation model. In the following description it is further assumed that the MPCs of interest interact in the far field of the antenna arrays, i.e., the individual paths can be modeled as plane waves.

A. Antenna Array Model

The antenna array model describes the angular and frequency dependency of the array transfer function. The transfer function of a Tx/Rx antenna array with $M_{T/R}$ ports, sampled at M_f fixed frequency points, P angles, and for the H (horizontal) or V (vertical) orthogonal polarization component for a far field plane wave signal, is defined as a three dimensional complex-valued tensor

$$\mathcal{B}_{H/V}^{(T/R)}(\boldsymbol{\varphi}_{T/R}, \boldsymbol{\vartheta}_{T/R}) \in \mathbb{C}^{M_{T/R} \times M_f \times P}. \tag{1}$$

The two vectors $\boldsymbol{\varphi}_{T/R} \in [-\pi \ \pi[^{P\times 1}$ and $\boldsymbol{\vartheta}_{T/R} \in [-\pi/2 \ \pi/2]^{P\times 1}$ contain P angles for azimuth and elevation, respectively. The antenna array description (1) can be obtained, e.g., through a calibration measurement, where the whole antenna array is rotated w.r.t. a defined reference point, and the frequency response of each antenna element is measured for a sufficient number of angles. Interpolation to an arbitrary angle can be achieved, e.g., through a Fourier series representation, such as Effective Aperture Distribution Function (EADF) [21], [22]. The EADF also provides efficient means to obtain the derivatives, required by the estimation algorithm described in Section IV.

For the experiments in this paper, a virtual antenna array is employed. A virtual array is formed by moving a single antenna such that its different positions form an array. This method not only reduces the hardware requirements, but also has the added benefit of being free from mutual coupling effects; on the downside, the channel to be measured by the array has to stay static for the duration that is required to move the antenna to all its positions. The model (1) for the virtual array can be constructed by first obtaining the angular-frequency response for the single antenna $b_{ref}(\varphi, \vartheta, f)$, defined at the origin of the coordinate system. The response of the i^{th} virtual antenna element, having a position vector $\mathbf{r}_i^{\mathrm{T}} = [x_i \ y_i \ z_i]$, and a rotation $\{\tilde{\varphi}_i, \tilde{\vartheta}_i\}$, is given by

$$b_i(\varphi, \vartheta, f) = \mathrm{e}^{\mathrm{j}2\pi \frac{f}{c} \cdot \mathbf{r}_i^{\mathrm{T}} \cdot \mathbf{u}(\varphi,\vartheta)} b_{ref}(\varphi - \tilde{\varphi}_i, \vartheta - \tilde{\vartheta}_i, f) \tag{2}$$

where $\mathbf{u}(\varphi, \vartheta) = [\cos(\varphi)\cdot\cos(\vartheta) \ \ \sin(\varphi)\cdot\cos(\vartheta) \ \ \sin(\vartheta)]^{\mathrm{T}}$ is the unit vector in the direction φ, ϑ. Note that the frequency dependency in (2) results both from the directional frequency response of a single antenna, as well as the phase evolution at different frequencies according to the antenna's position in the array.

B. Double Directional Propagation Path Model

A realization of the multidimensional UWB MIMO channel tensor $\mathcal{H} \in \mathbb{C}^{M_R \times M_T \times M_f}$ is defined as the frequency domain transfer function of the channel between each MIMO antenna pair measured at the antenna feeds, see Figure 1. The propagation between the two antenna arrays is described as a superposition of P discrete MPCs $\mathrm{vec}\,(\mathcal{H}) = \sum_p \mathbf{h}_p$. The model for a single path is illustrated in Figure 1b and is given by

$$\mathbf{h}_p = \gamma_{ij,p} \cdot \sum_{ij} \mathrm{vec}\left(\mathbf{B}_i^{(T)}(\varphi_{T,p}, \vartheta_{T,p}) \lozenge \mathbf{B}_j^{(R)}(\varphi_{R,p}, \vartheta_{R,p}) \lozenge \left(\mathbf{b}^{(f)}(\tau_p) \right)^{\mathrm{T}} \right) \tag{3}$$

where $\lozenge$ denotes Khatri-Rao (column-wise Kronecker) product, $\mathbf{B}_{i/j}^{(T/R)}(\varphi_{T/R,p}, \vartheta_{T/R,p}) \in \mathbb{C}^{M_{T/R} \times M_f}$ is a matrix slice of (1) for a single direction (that of path p), and $\mathbf{b}^{(f)}(\tau) \in \mathbb{C}^{M_f \times 1}$ is the frequency response (phase shifts) resulting from the delay τ_p. The variable $\gamma_{ij,p}$ denotes the complex path weight of the $ij \in \{HH, HV, VH, VV\}$ polarization component. Note that for free space propagation, as well as reflections from materials such as large metallic surfaces, the phase shift and attenuation from the propagation channel (excluding the antennas) can be considered frequency independent. However, for more complex propagation mechanisms, a frequency dependent path weight model may be required [17]; this is not taken into account in the remainder of the paper. Possible effects of neglecting frequency-dependent propagation would be the occurrence of "ghost components". The wideband path model (3) differs from the well know narrowband model, see e.g. [23], in that the antenna array responses are frequency dependent. Hence, the response of a single path is no longer an outer product (or Kronecker product) of the steering vectors of the individual sampling apertures.

The superposition of the MPCs (3) can be expressed as

$$\mathbf{h} = \underset{M\times PN_{pol}}{\text{reshape}}\ {}^{3}\left\{ \underset{[3\ 1\ 4\ 2]}{\text{permute}}\ {}^{2}\left\{ \underset{M_T M_R \times N_{pol} \times M_f \times P}{\text{reshape}}\ {}^{1}\left\{ \begin{bmatrix} \mathbf{B}_H^{(R)} \lozenge \mathbf{B}_H^{(T)} \\ \mathbf{B}_V^{(R)} \lozenge \mathbf{B}_H^{(T)} \\ \mathbf{B}_H^{(R)} \lozenge \mathbf{B}_V^{(T)} \\ \mathbf{B}_V^{(R)} \lozenge \mathbf{B}_V^{(T)} \end{bmatrix} \lozenge \mathrm{vec}\left(\mathbf{B}^{(f)} \right)^{\mathrm{T}} \right\}_1 \right\}_2 \right\}_3 \cdot \boldsymbol{\gamma} \in \mathbb{C}^{M\times 1} \tag{4}$$

where $\mathbf{B}_{H/V}^{(R/T)} = \underset{M_{R/T}\times M_f P}{\text{reshape}} \left\{ \mathcal{B}_{H/V}^{(T/R)}(\boldsymbol{\varphi}_{T/R}, \boldsymbol{\vartheta}_{T/R}) \right\}$ and $\mathbf{B}^{(f)}(\boldsymbol{\tau}) = \left[\mathbf{b}^{(f)}(\tau_1) \ \ldots \ \mathbf{b}^{(f)}(\tau_P) \right] \in \mathbb{C}^{M_f \times P}$ contain the responses for P paths, and $\boldsymbol{\gamma} = \left[\ \boldsymbol{\gamma}_{HH}^{\mathrm{T}} \ \ \boldsymbol{\gamma}_{HV}^{\mathrm{T}} \ \ \boldsymbol{\gamma}_{VH}^{\mathrm{T}} \ \ \boldsymbol{\gamma}_{VV}^{\mathrm{T}} \ \right]^{\mathrm{T}} \in \mathbb{C}^{PN_{pol}\times 1}$, where N_{pol} denotes the number of polarization coefficients (here $N_{pol} = 4$).

III. Experimental Setup

The experiment aims at a reproducible measurement of a UWB channel in an environment with a breathing human. The measurement was performed using a Vector Network Analyzer (VNA) and a virtual antenna array, i.e., a single antenna was moved using a high precision positioner. The VNA was calibrated to the antenna feed points, and a stepped frequency sweep was conducted for 801 points on the 2–8 GHz frequency range, see Table I. These measurements are time consuming, and can not be used for real time measurement of a human subject. They serve only as a proof-of-principle; real-time measurements could be performed with real arrays, excited by short large-bandwidth signals, such as chirps or impulses.

Two types of measurements were performed. In the first ones, an object that reflects similar amount of RF radiation as a human was positioned in a controlled manner, imitating the movement of the chest while breathing. Another measurement was performed with a human subject, who was holding his

breath during inhale/exhale periods for the duration of each VNA frequency sweep at each antenna position. Before each measurement, a reference measurement was taken without the object of interest inside the chamber to facilitate background removal in the post-processing of the data, discussed in Section IV.

A. UWB Antennas and the Virtual Array

The antennas used in the measurements are custom built UWB antennas [24], [25], shown in Figure 2a. The frequency response of the antennas as a function of azimuth angle (elevation fixed to horizontal plane) are obtained by a calibration measurement, and the magnitudes in the range 0.05–16 GHz are shown in Figures 2b and 2c. The color scale can be interpreted directly as magnitude (attenuation in dB) of the complex transfer function of the antenna for a far field plane wave. The planar monopole antenna[1] is preferred over the UWB horn [25] due to its omnidirectional beampattern for situations where the location of the object is not known a priori. However, the frequency range where the omnidirectionality applies is limited to approximately 2.2–7.3 GHz. In the measurements, different combinations of these antennas were used based on their suitability and availability.

Figure 3 illustrates the ambiguity function of a virtual 10-element uniform linear antenna array (ULA-10) with $d = 5$ cm antenna spacing, using the planar monopole antenna at 2.2–7.3 GHz. The ambiguity function is defined as

$$C(\varphi_i, \varphi_j) = \frac{\text{vec}\left(\mathbf{B}(\varphi_i)\right)^{\text{H}} \text{vec}\left(\mathbf{B}(\varphi_j)\right)}{\|\text{vec}\left(\mathbf{B}(\varphi_i)\right)\|_F \|\text{vec}\left(\mathbf{B}(\varphi_j)\right)\|_F} \tag{5}$$

where $\mathbf{B}(\varphi_i) \in \mathbb{C}^{M_{T/R} \times M_f}$ is defined as in (1), and reduces to a narrowband steering vector $\mathbf{b}(\varphi_i) \in \mathbb{C}^{M_{T/R} \times 1}$ for a single frequency. Figure 3 compares the ambiguity of the wideband model to the narrowband ones at lowest and highest frequency. It can be observed that the wideband array steering vectors do not suffer from angular ambiguity, or grating lobes, which occur for narrowband steering vectors should the antenna spacing exceed $\lambda/2$, see e.g. the plot at 7.3 GHz where $d \approx 1.2\lambda$. This stems from the fact that the grating lobes for different frequencies occur at different angles. Hence their influence is effectively reduced using the wideband modeling. Furthermore, the angular resolution, i.e., the width of the main lobe is much narrower for the wideband case than the lowest frequency alone. It should be mentioned that one can achieve acceptable wideband ambiguity properties even with significantly smaller number of antennas. However, such analysis is outside the scope of this paper. For discussion on ultrawideband arrays, see e.g. [26], [27].

B. Measurement with Artificial "Breathing" Object

The measurement setup is summarized in Table I, and illustrated in Figure 4. Two linear positioners, one for the uniform linear antenna array (ULA) and one for the breathing object, were placed inside the anechoic chamber at UltRa Lab [28]. The positions of the Rx antenna and the object, as well as the frequency sweep of the VNA, were controlled by a Labview script on a PC.

Figure 4a shows the approximate layout of the anechoic chamber. Two static scatterers (metallic poles) were placed

[1]The planar monopole antenna follows the design of solution A, listed in [24, Table I].

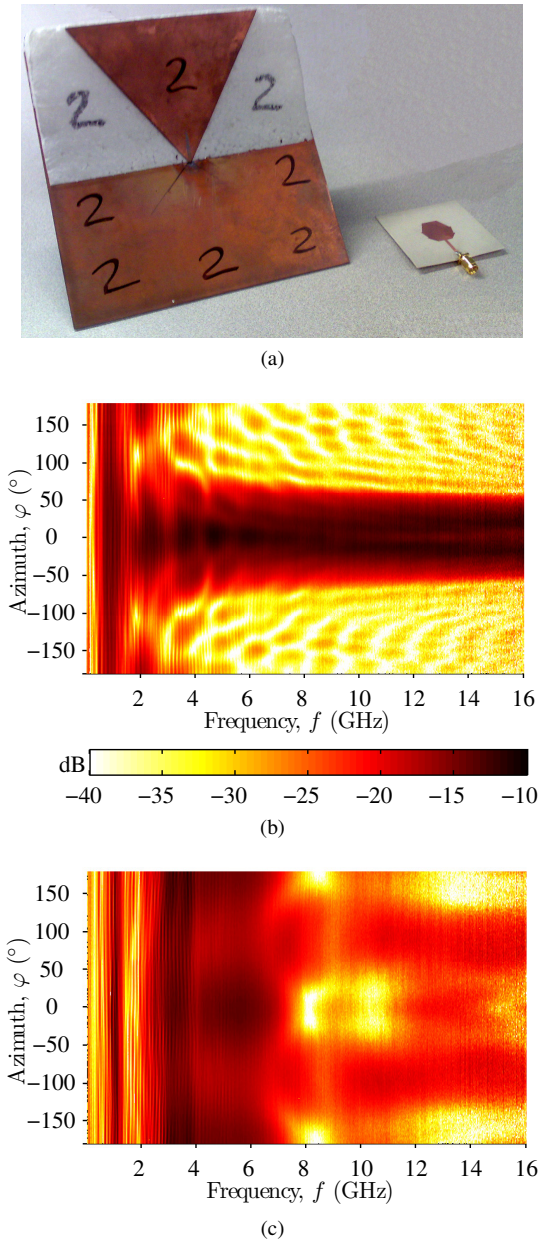

Fig. 2: (a) Antennas used in the measurements, along with the magnitudes (in dB) of their (V-polarized) angular frequency responses for (b) UWB horn antenna, and (c) UWB planar monopole antenna.

TABLE I: Measurement parameters.

Rx Array configuration	10-element virtual ULA, 5 cm spacing
VNA, HP 8720ET	2–8 GHz, 801 points, IF BW 300 Hz, "Stepped frequency sweep" mode
"Breathing" object	Two aluminium foiled basketballs at 8 positions over a ± 15 mm sinusoidal path.

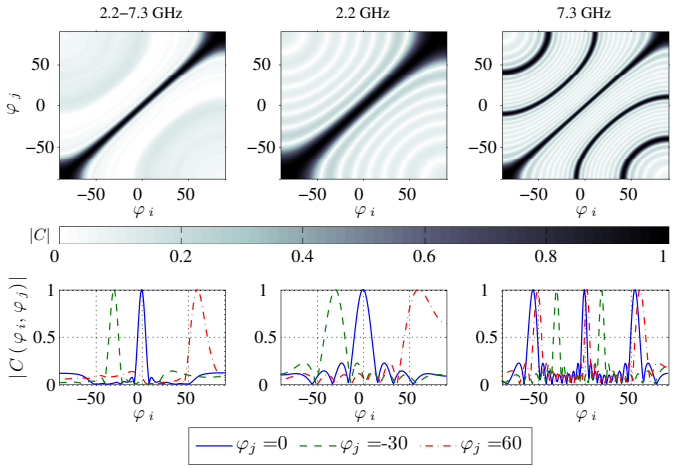

Fig. 3: Ambiguity function of a ULA-10 UWB (2.2–7.3 GHz) antenna array model compared to narrowband model at 2.2 GHZ and 7.3 GHz.

TABLE II: Potential signal routes for Rx1 position in the anechoic chamber, see Figure 4a. S1 and S2 refer to the scatterers, and B (ball) denotes the object.

Route	Length (m)	Angle, φ_R (°)
A: Tx–S1–B–Rx1	8.88	31
B: Tx–S2–B–Rx1	9.92	31
C: Tx–B–Rx1	8.25	31
D: Tx–B–S2–Rx1	10.32	13

in the chamber to create (controlled) multipath propagation. The Rx array positioner was sequentially placed in each corner of the chamber, and each measurement was repeated in non-line-of-sight (NLOS) conditions by blocking the line-of-sight (LOS) between the Tx and the object using a metallic bookshelf. LOS measurements were conducted using UWB horn antennas, whereas NLOS measurements were performed with UWB planar antennas. In this paper results from Rx1 position only, corresponding to Figure 4, are reported. The path lengths and angles based on the measured center points of the interacting objects are listed in Table II.

Before the actual measurement, a test measurement was performed in order to find a suitable object to be used in the measurement to replace a human. Figure 5 illustrates the test results by comparing the signal level reflected from different objects. Based on this test, a setup with two basketballs covered by aluminum foil was chosen as the "breathing" object.

C. Measurement with a Human Subject

The measurement with a human subject was limited to one Rx array location (same 10-element ULA), and two "object" positions, namely "inhale" and "exhale". The test person was sitting inside the chamber in a comfortable chair, see Figure 6. At each virtual antenna array position, two measurements were taken, one for inhale and one for exhale. The person indicated his hold of breath, either with empty lungs, or lungs full of air, using a thumb operated light switch. Otherwise, he was immobile during the approximately 10 minute measurement.

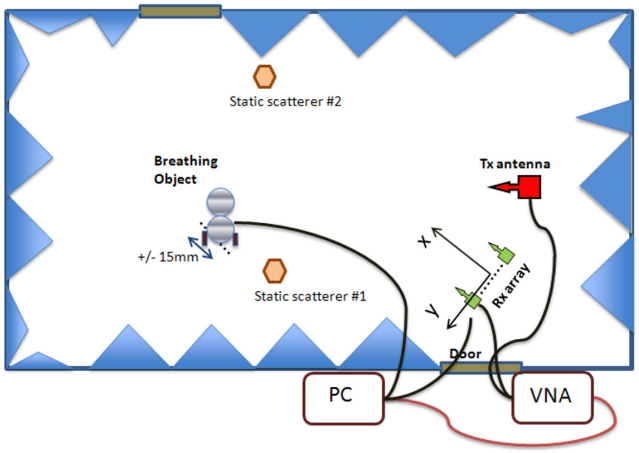

(a)

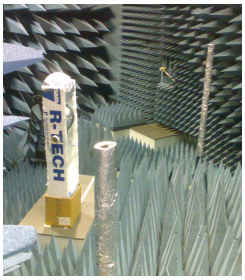

(b)

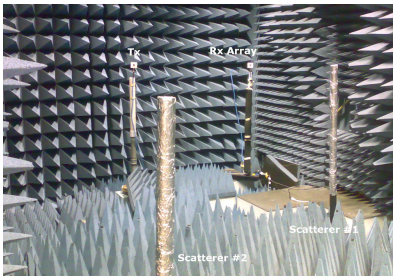

(c)

Fig. 4: (a) Measurement setup inside the anechoic chamber. (b) The breathing object and two scattering poles. (c) View from the opposite door.

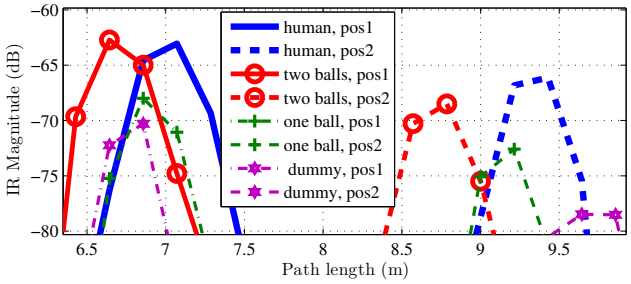

Fig. 5: Comparison of measured magnitude of the impulse response at 1.6–3 GHz from different types of objects: a human, one or two aluminium foil covered basketballs, and a small dummy. Two balls have the closest resemblance to that of human in terms of reflected signal level.

The measurement was repeated in NLOS conditions, while blocking the direct path between Tx and the person using a metallic bookshelf. In addition, each measurement was repeated so that the person had an aluminium foil wrapped around the chest. This facilitates the identification of the specific MPC, which corresponds to the reflection from the chest.

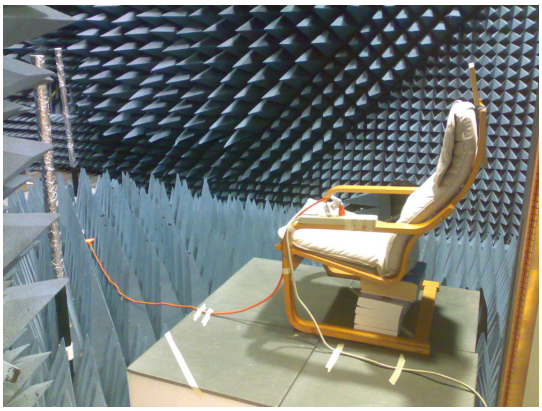

Fig. 6: Chair on which the person was sitting inside the chamber. Holding the breath was indicated by a light switch, attached on the armrest.

IV. Parameter Estimation

A. Reduced Measurement Model

For brevity, we describe the estimation methods w.r.t. a reduced measurement model, namely the one supporting the measurement setup described in Section III. The difference to the full model (4) is in that a (virtual) V-polarized[2] antenna array was employed at Rx only, whereas a single, V-polarized antenna was used as a transmitter. In addition, the employed virtual array was a uniform linear array, and hence the angular modeling is limited to the azimuthal plane. It is assumed that these assumptions do not significantly deteriorate the system performance in the studied anechoic chamber environment, however, this assumption does not hold in general, see e.g. [22] for a discussion. With these assumptions, the model for a single MPC reduces from (3) to

$$\tilde{\mathbf{h}}_p(\boldsymbol{\theta}_p) = \mathrm{vec}\left(\mathbf{B}^{(R)}(\varphi_{R,p}) \Diamond \mathbf{b}^{(f)^{\mathrm{T}}}(\tau_p)\right) \cdot \gamma_{VV,p} \tag{6}$$

and the superposition of P paths can be written as

$$\begin{aligned}\tilde{\mathbf{h}} &= \sum_p \mathbf{h}_p = \mathbf{B}(\boldsymbol{\tau}, \boldsymbol{\varphi}_R) \cdot \boldsymbol{\gamma} \in \mathbb{C}^{M_R M_f \times 1} \\ &= \underset{M_R M_f \times P}{\mathrm{reshape}} \left\{ \mathbf{B}^{(R)}(\boldsymbol{\varphi}_R) \Diamond \mathrm{vec}\left(\mathbf{B}^{(f)}(\boldsymbol{\tau})\right)^{\mathrm{T}}, \right\} \cdot \boldsymbol{\gamma}_{VV}.\end{aligned} \tag{7}$$

where $\mathbf{B}^{(R)}(\boldsymbol{\varphi}_R) = \underset{M_R \times M_f P}{\mathrm{reshape}} \left\{ \mathcal{B}^{(R)}(\boldsymbol{\varphi}_R) \right\}$. The parameter vector for P paths and $L = 4$ parameters can be defined as

$$\boldsymbol{\theta} = [\boldsymbol{\tau}^{\mathrm{T}} \ \boldsymbol{\varphi}_R^{\mathrm{T}} \ \boldsymbol{\alpha}^{\mathrm{T}} \ \boldsymbol{\phi}^{\mathrm{T}}]^{\mathrm{T}} \in \mathbb{R}^{PL \times 1} \tag{8}$$

where the complex path weight γ is reparameterized into two real valued parameters α and ϕ as $\gamma = \mathrm{e}^{\alpha + \mathrm{j}\phi}$. A single snapshot of the measured channel realization is modeled as

$$\tilde{\mathbf{y}} = \tilde{\mathbf{h}} + \tilde{\mathbf{n}} \in \mathbb{C}^{M_R M_f \times 1} \tag{9}$$

where $\mathbf{n} \sim \mathcal{N}(\mathbf{0}, \tilde{\sigma}_n^2 \mathbf{I})$ is complex, circular symmetric white Gaussian measurement noise.

[2]The term V-polarized is used to highlight that the polarization alignment of the antennas was close to vertical.

B. Background removal

As we are only interested in estimating the influence of moving a specific object in the environment, we perform the following background removal from the measured channel frequency responses. Before the actual measurement, a reference channel $\mathbf{y}_{ref} \mathbb{C}^{M_R M_f \times 1}$ is measured for all M_R antenna positions, with the object or person of interest *not* being inside the chamber. The MPC parameter estimation is then conducted for a data set obtained by

$$\mathbf{y} = \tilde{\mathbf{y}} - \mathbf{y}_{ref} \tag{10}$$

where the reference channel $\mathbf{y}_{ref}$ is subtracted from the measured channel frequency response $\tilde{\mathbf{y}}$. Ideally, all remaining, significant components in the channel should result from interaction with the scattering object; note that this interaction can either create new MPCs, or block or attenuate existing ones. Hence, it is assumed that $\mathbf{y} \sim \mathcal{N}(\mathbf{h}', \sigma_n^2 \mathbf{I})$, where $\mathbf{h}'$ denotes the MPCs resulting from the interaction with the object. From (10), the delays τ and azimuth angles φ_R along with corresponding path weights γ are estimated for a number of paths.

C. Path Detection

The initialization of the parameter estimation is performed using a successive cancellation type of grid search, where the detection of paths is based on single path maximum likelihood (ML) criterion. The approach is similar to [29], generalized for the wideband antenna array model (2). Typically, this initialization is performed for a larger number of paths at the first snapshot, and for a few new paths at each snapshot. The objective of the ML is to maximize the likelihood function

$$p(\mathbf{y}|\boldsymbol{\theta}, \sigma_n^2) = \frac{1}{\pi^{\mathrm{M}} \sigma_n^{2M}} \mathrm{e}^{-\frac{1}{\sigma_n^2}(\mathbf{y} - \mathbf{h}(\boldsymbol{\theta}))^{\mathrm{H}} \cdot (\mathbf{y} - \mathbf{h}(\boldsymbol{\theta}))}. \tag{11}$$

Consequently, taking the logarithm of (11) and maximizing it w.r.t $\boldsymbol{\theta}$ yields

$$\begin{aligned}&\hat{\boldsymbol{\theta}}_{ML} = \\ &\arg\min_{\boldsymbol{\theta}} \left(\frac{1}{\sigma_n^2} \left(\mathbf{y} - \mathbf{B}(\boldsymbol{\tau}, \boldsymbol{\varphi}_R) \cdot \boldsymbol{\gamma}\right)^{\mathrm{H}} \left(\mathbf{y} - \mathbf{B}(\boldsymbol{\tau}, \boldsymbol{\varphi}_R) \cdot \boldsymbol{\gamma}\right) \right).\end{aligned} \tag{12}$$

As the path weights $\boldsymbol{\gamma}$ are linear in (7), their best linear unbiased estimate can be expressed as

$$\hat{\boldsymbol{\gamma}} = \left(\mathbf{B}^{\mathrm{H}} \mathbf{B}\right)^{-1} \mathbf{B}^{\mathrm{H}} \mathbf{y} \tag{13}$$

where $\mathbf{B} = \mathbf{B}(\boldsymbol{\tau}, \boldsymbol{\varphi}_R)$ in (7). Inserting (13) in (12) yields after some manipulation

$$\begin{bmatrix} \hat{\boldsymbol{\tau}} \\ \hat{\boldsymbol{\varphi}}_R \end{bmatrix}_{ML} = \arg\max_{\boldsymbol{\tau}, \boldsymbol{\varphi}_R} \left(\frac{1}{\sigma_n^2} \left(\mathbf{y}^{\mathrm{H}} \mathbf{B}\right) \left(\mathbf{B}^{\mathrm{H}} \mathbf{B}\right)^{-1} \left(\mathbf{B}^{\mathrm{H}} \mathbf{y}\right) \right). \tag{14}$$

Evaluating (14) for a single path, and assuming the non-polarimetric wideband path model (6), the ML criterion reduces to

$$C(\boldsymbol{\theta}_p, \mathbf{y}) = \frac{1}{\sigma_n^2} \left| \frac{\mathbf{b}^{\mathrm{H}}(\boldsymbol{\theta}_p)}{\sqrt{\mathbf{b}^{\mathrm{H}}(\boldsymbol{\theta}_p) \mathbf{b}(\boldsymbol{\theta}_p)}} \mathbf{y} \right|^2 \tag{15}$$

where $\mathbf{b}(\boldsymbol{\theta}_p) = \mathrm{vec}\left(\mathbf{B}^{(R)}(\varphi_{R,p}) \Diamond \mathbf{b}^{(f)}(\tau_p)^{\mathrm{T}}\right)$. A new path estimate $\boldsymbol{\theta}_n$ is obtained as the set of parameters maximizing (15), and then solving for (13). The influence of this path can be subtracted from the data as $\mathbf{y}' = \mathbf{y} - \mathbf{h}(\boldsymbol{\theta}_n)$, and the procedure may be repeated to detect more paths. It is also possible to optimize the already obtained path estimates jointly between detections, using the algorithm outlined in the next section.

Equation (15) can also be interpreted as a matched filter, or a generalized beamformer, and the objective is to find the parameters $\boldsymbol{\theta}_p$ that maximize the correlation with the measurement. Note that by setting $\sigma_n^2 = 1$, equation (15) can also be interpreted as the multidimensional power profile of the propagation channel. This has been used for the illustrations in Section V. An example of a computationally efficient implementation of a grid search over the parameters τ and φ_R for evaluating (15) is outlined in the Appendix.

D. Parameter Optimization

The initialization of the path estimates is based on a suboptimal strategy of successive detection and cancellation using of the ML criterion for a single-path only (15). Therefore, it is necessary to perform *joint* optimization of the estimates. It can be shown that finding the joint ML estimate of the parameters $\boldsymbol{\theta}$ in (8) equals

$$\hat{\boldsymbol{\theta}}_{ML} = \arg\min_{\boldsymbol{\theta}} \frac{|| \left(\mathbf{y} - \mathbf{h}(\boldsymbol{\theta})\right) ||_F^2}{\sigma_n^2}. \tag{16}$$

No closed form solution exist for this nonlinear least squares optimization problem, so we resort to an iterative optimization technique, namely the Levenberg-Marquardt method [30], which is also used for a narrowband signal model in the RIMAX algorithm [16]. As the algorithm is gradient-based, it requires the derivatives of the data model (7) w.r.t. the estimated parameters (8). Let us define the Jacobian matrix as $\mathbf{D}(\boldsymbol{\theta})$, the Score function $\mathbf{q}(\mathbf{y}|\boldsymbol{\theta})$, and the Fisher Information Matrix $\mathbf{J}(\boldsymbol{\theta})$ as

$$\mathbf{D}(\boldsymbol{\theta}) = \left[\frac{\partial}{\partial\theta_1}\mathbf{h}(\boldsymbol{\theta}) \ \cdots \ \frac{\partial}{\partial\theta_{LP}}\mathbf{h}(\boldsymbol{\theta})\right] \in \mathbb{C}^{M_R M_f \times LP} \tag{17}$$

$$\begin{aligned}\mathbf{q}(\mathbf{y}|\boldsymbol{\theta}) &= \left[\frac{\partial}{\partial\theta_1}\mathcal{L}(\mathbf{y}|\boldsymbol{\theta}) \ \cdots \ \frac{\partial}{\partial\theta_1}\mathcal{L}(\mathbf{y}|\boldsymbol{\theta})\right]^{\mathrm{T}} \\ &= \frac{2}{\sigma_n^2} \cdot \Re\left\{\mathbf{D}^{\mathrm{H}}(\boldsymbol{\theta})(\mathbf{y} - \mathbf{h}(\boldsymbol{\theta}))\right\} \in \mathbb{R}^{LP\times 1}\end{aligned} \tag{18}$$

$$\begin{aligned}\mathbf{J}(\boldsymbol{\theta}) &= -\mathcal{E}\left\{\frac{\partial}{\partial\boldsymbol{\theta}^{\mathrm{T}}}\mathcal{L}(\mathbf{y}|\boldsymbol{\theta}) \cdot \left(\frac{\partial}{\partial\boldsymbol{\theta}^{\mathrm{T}}}\mathcal{L}(\mathbf{y}|\boldsymbol{\theta})\right)^{\mathrm{T}}\right\} \\ &= \frac{2}{\sigma_n^2} \cdot \Re\left\{\mathbf{D}^{\mathrm{H}}\mathbf{D}\right\} \in \mathbb{R}^{LP\times LP}\end{aligned} \tag{19}$$

where $\mathcal{L}(\mathbf{y}|\boldsymbol{\theta})$ denotes the log-likelihood function. The estimates are then optimized by iterating

$$\hat{\boldsymbol{\theta}}^{\{i+1\}} = \hat{\boldsymbol{\theta}}^{\{i\}} + \left(\mathbf{J}(\boldsymbol{\theta}^{\{i\}}) + \zeta^{\{i\}}\mathbf{I} \odot \mathbf{J}(\boldsymbol{\theta}^{\{i\}})\right)^{-1} \mathbf{q}(\mathbf{y}|\boldsymbol{\theta}^{\{i\}}) \tag{20}$$

where $\odot$ denotes element-wise matrix product. The step size tuning parameter $\zeta^{\{i\}}$ can be decreased if the iteration improved the fit (16), otherwise $\zeta^{\{i\}}$ should be increased, see [16] for discussion. Convergence can be evaluated, e.g., by testing if $(\hat{\boldsymbol{\theta}}^{\{i+1\}} - \hat{\boldsymbol{\theta}}^{\{i\}})^2$ is smaller than 10% of the Cramér-Rao bound, obtained from the diagonal values of $\mathbf{J}^{-1}(\boldsymbol{\theta})$ in (19).

After convergence, it is possible to either detect more paths from the residual $\mathbf{y} - \mathbf{h}(\boldsymbol{\theta})$, or use the current estimates as the initial values for the next snapshot of data.

V. Results

A. Results with the Object — LOS Case

This section describes results from a measurement, where the breathing object (two aluminum foil covered basketballs) was moved to eight positions in the range ± 15 mm, see Figure 4. Figure 7 shows the Power-Angular-Delay Profile (PADP) of the measurement, evaluated using (15) with $\sigma_n^2 = 1$ and averaged over the eight measured ball positions. Some residual signal can still be observed after the reference channel cancelation (10), especially at the LOS between the antennas around path lengths of less than 2 m, as well as for Scatterer #1 after 4 m path length. Figure 7c shows the PADP zoomed at the paths of interest. Also some of the probable signal routes are identified. The white crosses drawn over the PADP denote the locations of estimated MPCs. When comparing the path lengths from Table II, it should be noted that the basketball has a radius of about 12 cm, and the scattering poles about 3 cm, which shorten the actual path length compared to measured object center points. In addition, a separate calibration was performed to determine the effect of the signal delay of the pair of UWB horn antennas to the path length estimate. This calibration resulted in an increase by 11 cm compared to the physical distance between the antennas.

We limit the discussion to evaluating the strongest MPC resulting from the direct reflection from the object. Figure 7d shows the corresponding PADPs for the eight individual snapshots. The small white crosses denote the position of the ML estimate of the strongest MPC. It can be observed that the sinusoidal movement of the ball is well captured by the path estimate. Comparing the estimate of the path length $\hat{\tau} \cdot c \approx 8.12$ m in Figure 7d to the signal routes in Table II, it can be seen that it matches well with the direct path (route C) with 8.25 m - 0.24 m + 0.11 m = 8.12 m, after compensating -24 cm (twice the radius) for the reflection on the surface of the basketball, and adding +11 cm due to electric length of the antennas.

Figure 8 illustrates the evolution of the estimated path length difference (or differential delay, $\Delta\tau_k = \hat{\tau}_k - \bar{\tau}$) as well as the path weight phase difference ($\Delta\phi_k = \hat{\phi}_k - \bar{\phi}$) of the strongest MPC along with the known relative object displacement Δx. It can be observed that the relative delays and phases capture well the sinusoidal trend in the true displacement of the object. Note that although the axes are in the same scale (in mm), the influence of the object displacement on the path length depends on the projection of the displacement direction w.r.t. the angle to both the transmitter and the receiver, i.e. $0 \leq |\Delta\tau \cdot c|/|\Delta x| \leq 2$, where c denotes the speed of light. Note also that the obtained path length resolution is much higher than $c/B \approx 0.05$ m, assumed e.g. in [10]. In fact, the estimation error standard deviations in Figure 8b, obtained as the square root

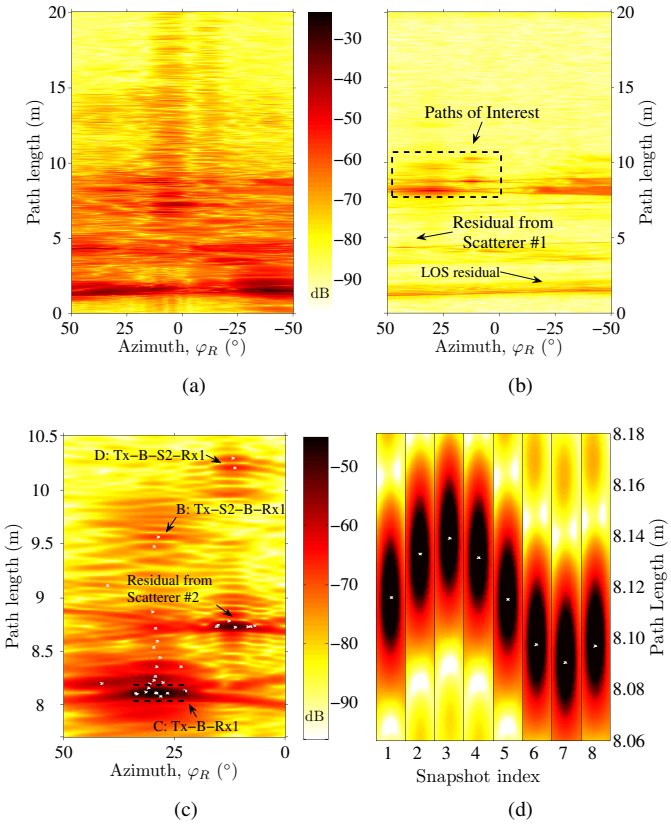

Fig. 7: (a) Power-Angular-Delay Profile (PADP) of the measurement averaged over the eight snapshots (ball positions). (b) PADP of **y**, see (10), i.e., after background removal. (c) PADP zoomed to the area of interest. White x-marks indicate estimated path components (36 in total). (d) PADP at the direct reflection for the eight snapshots.

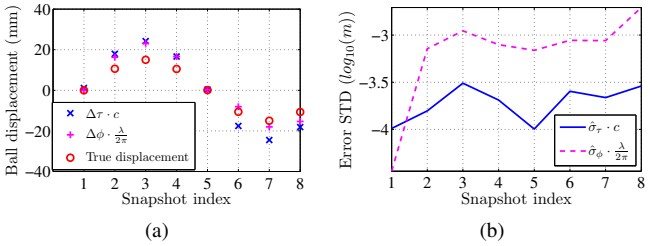

Fig. 8: (a) Breathing object displacement, the estimated path length difference of the strongest path ($\Delta\tau \cdot c$), and the mapping of the path weight phase difference (using $\lambda = c/f_c$, with $f_c = 5.0$ GHz) into equivalent distance ($\Delta\phi \cdot \lambda/2\pi$). (b) Estimation error standard deviation for both the delay $\hat{\sigma}_\tau$ and the phase $\hat{\sigma}_\phi$ mapped on the path length. The estimates are obtained from the inverse of (19), see [16] for discussion.

of the diagonal values of the inverse of the Fisher Information Matrix (19), indicate that the estimation error can be expected to be in the order of 1 mm.

B. Results with the Object — NLOS Case

In the NLOS measurement, a metallic bookshelf was placed between the Tx antenna and the breathing object. Also, the

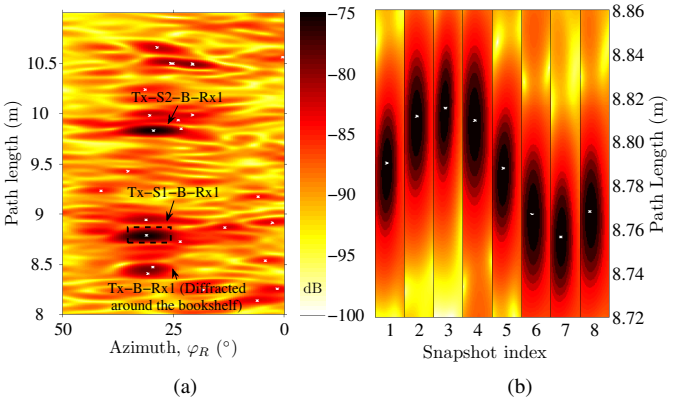

Fig. 9: PADPs for the NLOS case. White x-marks indicate estimated path components. (a) PADP of the overall area of interest averaged over the eight snapshots. (b) PADP at the strongest component (route A in Table II).

omnidirectional UWB planar antennas, see Figure 2, were employed instead of the UWB horns. The pair of UWB planar antennas was determined to have an electric length equivalent to 16 cm increase in the MPC path length.

Figure 9 shows the zoomed PADP of the NLOS measurement, comparable to Figures 7c and 7d. The strongest component can be identified to be the one corresponding to route A in Table II, with $\hat{\tau} \cdot c \approx 8.79$ m, while the measured path length for route A after corrections (diameters of the pole, 0.06 m, and the ball, 0.24 m, electric length of the antenna pair, 0.16 m) should have been 8.88 m - 0.06 m - 0.24 m + 0.16 m = 8.74 m. The 5 cm difference may result, e.g., from tilting of the Scatterer #1 pole and other uncertainties. However, it can be observed that the movement of the object is very well captured by the path delay estimate, shown as the white cross at the maximum of the PADP in Figure 9b.

It should be noted, although not explicitly shown here, that both for LOS and NLOS cases it is possible to identify several other MPCS whose parameters capture the sinusoidal trend of the object movement. On the other hand, there are also many MPCs that do not reveal such information, either due to poor angle of reflection w.r.t. the direction of movement, or the fact that those paths are residual errors from the background removal. Nevertheless, whenever such a trend is observed, it could be used in identifying the MPCs interacting with the target, and the path parameters could be further utilized for target localization.

C. Results with a Human Target

Figure 10 shows the PADP of the measurement with the human target before (Figure 10a) and after (Figure 10b) background removal. The measurement setup was improved (compared to measurements in Sections V-A and V-B) by stabilizing the cable while the positioner was moving. This results in smaller residual error after background removal in Figure 10b compared to Figure 7b. Figures 10c and 10d show a comparison of the PADPs and MPC estimates in two separate measurements, where the only difference is that in Figure 10d,

an aluminium foil was wrapped around the chest of the test subject. This resulted in a stronger reflection, which helps to identify the sources of the peaks in the PADPs, as indicated in the figures. Figure 10e illustrates the estimated MPCs in the range of chest and head. It can be observed that, in addition to a path length change of about 3 cm (corresponding to about 1.5 cm chest displacement), even a slight angular shift during inhale and exhale periods is captured in the MPC estimate (P3), whereas the estimate from the head reflection MPC (P1) remains more or less constant.

Figure 11 shows the PADP and MPC estimates from the human measurement in NLOS, while a metallic bookshelf was blocking the LOS between Tx and the test subject. It can be observed that the estimated MPC (P2, denoted by green x-mark) of the reflection from the chest converged to another, weaker, maximum at the second snapshot, and a new path (P21) was detected for the chest location. The path length difference of the old (P2: $\hat{\tau} \cdot c = 12.01$ m) to the new estimate (P21: $\hat{\tau} \cdot c = 12.05$ m) is 4 cm, corresponding to a chest displacement of about 2 cm, whereas the head component remains at a constant path length (P1: $\hat{\tau} \cdot c = 12.12$ m). It should be noted that in a real system, the sampling rate would be much higher than two samples per breath cycle; hence, it would be possible to employ a state-space model along with sequential estimation technique to track the MPCs over time [29].

VI. Conclusions

UWB signalling combined with MIMO processing enables a radar having very high delay resolution as well as angular information. This paper presented a study on UWB propagation for estimating small scale movement such as human respiratory activity. A model based on a superposition of MPCs, along with a wideband antenna array model was employed. We showed that the wideband antenna array model does not suffer from ambiguities, which are present for narrowband signal models, even if the antenna spacing is not strictly less than half a wavelength. Measurements were performed under ideal conditions in an anechoic chamber with a VNA and a virtual antenna array, using both an artificial "breathing object" as well as a human subject. After removal of the static background, the MPCs resulting from the interaction with the test objects were estimated and analyzed. The displacement of the artificial object, as well as the human chest while breathing, were captured non-intrusively from about 5 m distance. Based on the results, it may be possible to develop a system where the breathing rate of a person within a room could be determined. The information of angles and delays corresponding to the propagation paths showing such movement, possibly also from NLOS paths, and potentially observed with multiple receiver units, could be used to determine and track the position of the person(s) in a room. However, additional effort is required to study the performance of the envisioned system in realistic SNR conditions obtainable with a practical UWB setup. Further research should also be put on determining a good trade-off between the signal bandwidth and the number of antennas.

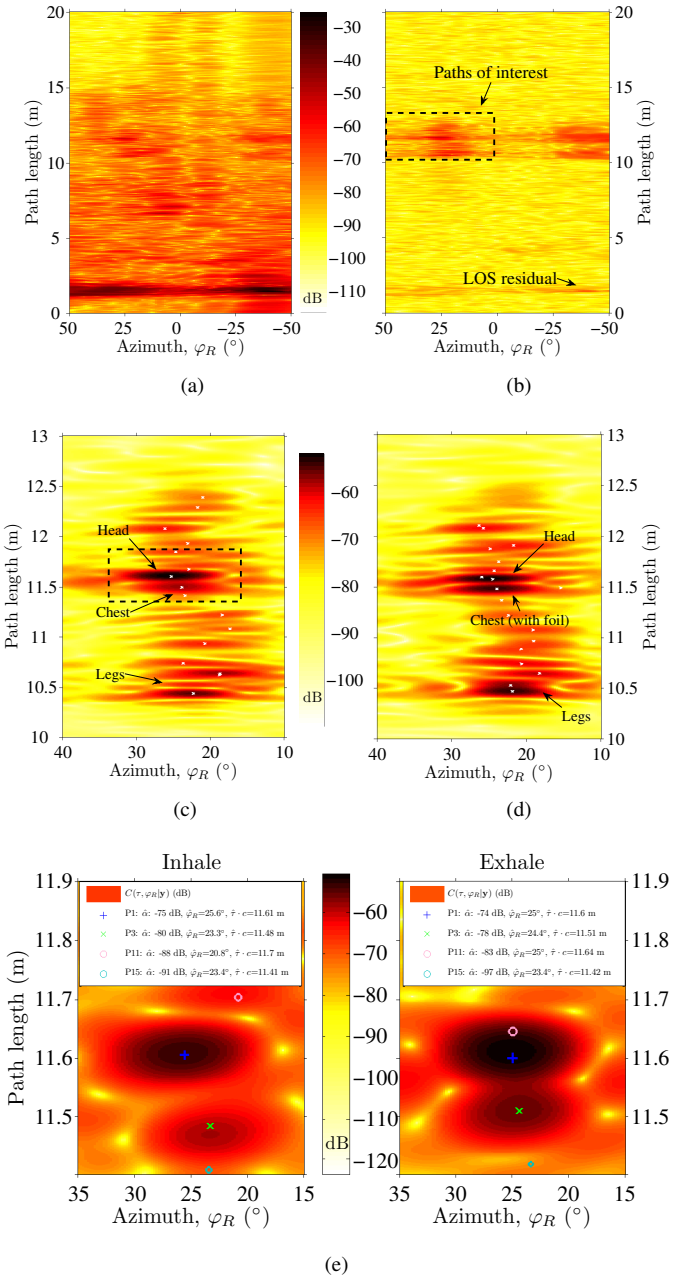

Fig. 10: PADPs of the measured channel for the human target. (a) and (b) are averaged over the two (inhale and exhale) snapshots and have the same color scale. (a) is before, and (b) is after background removal. (c) shows the PADP zoomed into the area of interest. (d) is the same as (c), but from a repeated measurement with aluminium foil around the chest. (e) illustrates the estimated propagation paths in the range of chest and head for the two snapshots.

Appendix
Wideband Data Transformation

Wideband Data Transformation (WBDT) is a computationally efficient solution for evaluating the single path, single polarization ML criterion (15), e.g., for path detection or power profile estimation purposes. The idea is to employ the

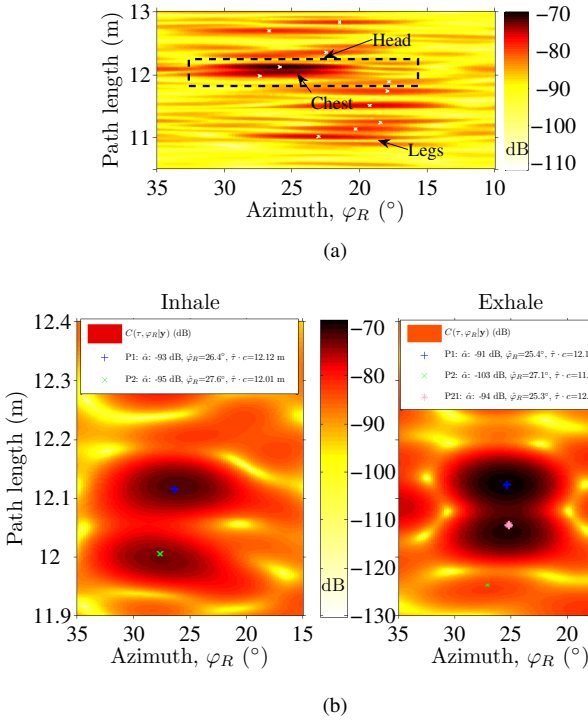

(a)

(b)

Fig. 11: PADP of the human target measurement in NLOS conditions. (a) PADP zoomed into the area of interest. (b) Estimated propagation paths in the range of chest and head for the two snapshots. It can be observed that the chest estimate of the inhale snapshot converged to another maximum, and a new path was detected at the chest position in the exhale snapshot.

wideband array responses (steering vectors) of the antenna array(s) to transform the data from the samples collected at the antenna feeds into angular domain, and in the end employing the frequency domain steering vectors to transform into delay domain. This can be viewed as transformation from the MIMO channel tensor observed at the antenna ports, see Figure 1a, into a sampling grid defined by the geometrical parameters, see Figure 1b. For simplicity, we limit the discussion here to the reduced data model (7), i.e., Rx array only.

The approach proceeds as follows, let us have a measurement (or residual) vector (10) in matrix form as

$$\underset{M_f \times M_R}{\mathbf{Y}} = \text{reshape}\left\{\mathbf{y}\right\} \tag{21}$$

as well as the wideband response functions

$$\mathbf{B}_d^{(f)}(\boldsymbol{\tau}_d) \in \mathbb{C}^{M_f \times N_f} \tag{22}$$

$$\mathcal{B}_d^{(R)}(\boldsymbol{\varphi}_d) \in \mathbb{C}^{M_R \times M_f \times N_R} \tag{23}$$

for frequency domain with N_f delay detection points, and Rx array with N_R angular detection points, respectively. Furthermore, let as define the following transformation matrices $\mathbf{Q}_R \in \mathbb{C}^{M_f M_R \times N_R}$ and $\mathbf{Q}_f \in \mathbb{C}^{M_f \times N_f}$ as

$$\mathbf{Q}_R = \sqrt{M_f} \cdot \left[\frac{\text{vec}\left(\mathbf{B}_{d,1}^{(R)\,\mathrm{T}}\right)}{\left\|\text{vec}\left(\mathbf{B}_{d,1}^{(R)\,\mathrm{T}}\right)\right\|_F} \quad \cdots \quad \frac{\text{vec}\left(\mathbf{B}_{d,N_R}^{(R)\,\mathrm{T}}\right)}{\left\|\text{vec}\left(\mathbf{B}_{d,N_R}^{(R)\,\mathrm{T}}\right)\right\|_F} \right] \tag{24}$$

$$\mathbf{Q}_f = \left[\frac{\mathbf{b}_{d,1}^{(f)}}{\left\|\mathbf{b}_{d,1}^{(f)}\right\|_F} \quad \cdots \quad \frac{\mathbf{b}_{d,N_f}^{(f)}}{\left\|\mathbf{b}_{d,N_f}^{(f)}\right\|_F} \right] \tag{25}$$

where $\mathbf{B}_{d,n_R}^{(R)} = \mathbf{B}_d^{(R)}(\varphi_{R,d,n_R})$ is the n_R^{th} matrix slice of the tensor $\mathcal{B}_d^{(R)}$ (23) and $\mathbf{b}_{d,n_f}^{(f)} = \mathbf{b}_d^{(f)}(\tau_{d,n_f})$ is the n_f^{th} column of the matrix $\mathbf{B}_d^{(f)} \in \mathbb{C}^{M_f \times N_f}$ (22).

The data tensor is then transformed (filtered) from the measurement data to the parameter domain as follows

1) First, $\mathbf{Y} \in \mathbb{C}^{M_f \times M_R}$ is transformed from Rx array domain to Rx angular domain to obtain $\mathbf{Y}^{(R)} \in \mathbb{C}^{M_f \times N_R}$ as

$$\mathbf{Y}^{(R)} = \underset{N_R \times M_f}{\text{reshape}^{\,2}}\left\{ \underset{N_R M_f \times M_R}{\text{reshape}^{\,1}}\left\{ \mathbf{Q}_R^{\mathrm{H}} \lozenge \text{vec}\left(\mathbf{Y}\right)^{\mathrm{T}} \right\}_1 \cdot \mathbf{1}_{M_R} \right\}_2^{\mathrm{T}} \tag{26}$$

where $\mathbf{1}_{M_R}$ denotes an $M_R \times 1$ vector of all ones (used here to sum over M_R antenna elements).

2) Then, $\mathbf{Y}^{(R)}$ is transformed from frequency domain to delay domain $\mathbf{Y}^{(f,R)} \in \mathbb{C}^{N_f \times N_R}$ as

$$\mathbf{Y}^{(f,R)} = \mathbf{Q}_f^{\mathrm{H}} \cdot \mathbf{Y}^{(R)} \tag{27}$$

3) The matrix of detection values, or the power profile of the channel, whose elements are equivalent to (15), is obtained by

$$\mathbf{C}(\boldsymbol{\tau}_d, \boldsymbol{\varphi}_{R,d}) = \frac{1}{\sigma^2}\left(\mathbf{Y}^{(f,R)} \odot \mathbf{Y}^{*(f,R)}\right) \tag{28}$$

where $\mathbf{A} \odot \mathbf{B}$ denotes the element-wise product.

Acknowledgment

The authors would like to acknowledge the efforts of Dr. Xuesong Yang, Seun Sangodoyin, Junyang Shen, in helping to conduct the measurements, as well as thank Dr. SangHyun Chang in helping to set up the experiments, and Prof. Hossein Hashemi for many fruitful discussions. Dr. Terry Lewis is also acknowledged for designing and manufacturing the UWB horn antennas, and Lukas Baumgartel for manufacturing the UWB planar antennas. The first author would also like to thank Academy of Finland, Finnish Technology Promotion Foundation, and Walther Ahlström foundation for their financial support.

References

[1] J. Lin, "Noninvasive microwave measurement of respiration," *Proceedings of the IEEE*, vol. 63, no. 10, pp. 1530–1530, 1975.

[2] J. Silvious and D. Tahmoush, "UHF measurement of breathing and heartbeat at a distance," *IEEE Radio and Wireless Symposium (RWS)*, pp. 567–570, 2010.

[3] C. Li, J. Ling, J. Li, and J. Lin, "Accurate Doppler radar noncontact vital sign detection using the RELAX algorithm," *IEEE Transactions on Instrumentation and Measurement*, vol. 59, no. 3, pp. 687–695, 2010.

[4] D. Smardzija, O. Boric-Lubecke, A. Host-Madsen, V. Lubecke, I. Sizer, T., A. Droitcour, and G. Kovacs, "Applications of MIMO techniques to sensing of cardiopulmonary activity," *IEEE/ACES International Conference on Wireless Communications and Applied Computational Electromagnetics*, pp. 618–621, 2005.

[5] O. Boric-Lubecke, V. Lubecke, A. Host-Madsen, D. Samardzija, and K. Cheung, "Doppler radar sensing of multiple subjects in single and multiple antenna systems," *7th International Conference on Telecommunications in Modern Satellite, Cable and Broadcasting Services*, vol. 1, pp. 7–11, 2005.

[6] S. Sahinoglu, S. Gezici, and I. Guvenc, *Ultra-wideband Positioning Systems: Theoretical Limits, Ranging Algorithms, and Protocols*. Cambridge University Press, 2008.

[7] J. Sachs, "Ultra-wideband sensing: The road to new radar applications," in *11th International Radar Symposium (IRS)*, June 2010.

[8] E. Cianca and B. Gupta, "FM-UWB for communications and radar in medical applications," *Wireless Personal Communications*, vol. 51, no. 4, pp. 793–809, 2009.

[9] G. Ossberger, T. Buchegger, E. Schimback, A. Stelzer, and R. Weigel, "Non-invasive respiratory movement detection and monitoring of hidden humans using ultra wideband pulse radar," *International Workshop on Ultra Wideband Systems*, pp. 395–399, 2004.

[10] E. Conti, A. Filippi, and S. Tomasin, "On the modulation of ultra wide band pulse radar signal by target vital signs," in *International Symposium on Bioelectronics and Bioinformatics, ISBB 2009*, Melbourne, Australia, Dec. 2009.

[11] S. H. Chang, R. Sharan, M. Wolf, N. Mitsumoto, and J. Burdick, "UWB radar-based human target tracking," in *IEEE Radar Conference 2009*, May 2009.

[12] K. Ohta, K. Ono, I. Matsunami, and A. Kajiwara, "Wireless motion sensor using ultra-wideband impulse-radio," *IEEE Radio and Wireless Symposium (RWS)*, pp. 13–16, 2010.

[13] M. Steinbauer, A. Molisch, and E. Bonek, "The double-directional radio channel," *IEEE Antennas and Propagation Magazine*, vol. 43, no. 4, pp. 51–63, Aug. 2001.

[14] X. Liu, H. Leung, and G. Lampropoulos, "Effects of non-uniform motion in through-the-wall SAR imaging," *IEEE Transactions on Antennas and Propagation*, vol. 57, no. 11, pp. 3539–3548, Nov. 2009.

[15] M. Dehmollaian, M. Thiel, and K. Sarabandi, "Through-the-wall imaging using differential SAR," *IEEE Transactions on Geoscience and Remote Sensing*, vol. 47, no. 5, pp. 1289–1296, May 2009.

[16] A. Richter, "Estimation of radio channel parameters: Models and algorithms," Ph. D. dissertation, Technischen Universität Ilmenau, Germany, May 2005, ISBN 3-938843-02-0. [Online]. Available: www.db-thueringen.de

[17] A. F. Molisch, "Ultra-wide-band propagation channels," *Proceedings of the IEEE*, vol. 97, no. 2, pp. 353–371, Feb. 2009.

[18] R. Zetik, J. Sachs, and R. Thoma, "UWB short-range radar sensing — the architecture of a baseband, pseudo-noise UWB radar sensor," *IEEE Instrumentation Measurement Magazine*, vol. 10, no. 2, pp. 39 –45, Apr. 2007.

[19] J. Salmi, S. Sangodoyin, and A. F. Molisch, "High resolution parameter estimation for ultra-wideband MIMO radar," in *The 44th Asilomar Conference on Signals, Systems, and Computers*, Pacific Grove, CA, Nov. 2010.

[20] Mathworks. Matlab. [Online]. Available: http://www.mathworks.com

[21] M. Landmann, A. Richter, and R. Thomä, "DOA resolution limits in MIMO channel sounding," in *International Symposium on Antennas and Propagation and USNC/URSI National Radio Science Meeting*, Monterey, CA, Jun. 2004, pp. 1708–1711.

[22] M. Landmann, "Limitations of experimental channel characterization," Ph. D. dissertation, Technischen Universität Ilmenau, Ilmenau, Germany, Mar. 2008. [Online]. Available: http://www.db-thueringen.de

[23] J. Salmi, "Contributions to measeurement-based dynamic MIMO channel modeling and propagation parameter estimation," Ph. D. dissertation, Helsinki University of Technology, Dept. of Signal Processing and Acoustics, Espoo, Finland, Aug. 2009, report 10, ISBN: 978-952-248-018-7. [Online]. Available: http://lib.tkk.fi/Diss/2009/isbn9789522480194/

[24] X.-S. Yang, K. T. Ng, S. H. Yeung, and K. F. Man, "Jumping genes multiobjective optimization scheme for planar monopole ultrawideband antenna," *IEEE Transactions on Antennas and Propagation*, vol. 56, no. 12, pp. 3659–3666, 2008.

[25] T. Lewis, "An ultrawideband digital signal design with power spectral density constraints," Ph. D. dissertation, University of Southern California, Dept. of Electrical Engineering, Los Angeles, CA, Aug. 2010.

[26] F. Anderson, W. Christensen, L. Fullerton, and B. Kortegaard, "Ultra-wideband beamforming in sparse arrays," *IEE Proceedings-H*, vol. 138, no. 4, pp. 342–346, Aug. 1991.

[27] S. Ries and T. Kaiser, "Ultra wideband impulse beamforming: It is a different world," *Signal Processing*, vol. 86, no. 9, pp. 2198–2207, 2006.

[28] UltRa Lab, "Ultra-wideband radio laboratory," University of Southern California, Los Angeles, CA. [Online]. Available: http://ultra.usc.edu/

[29] J. Salmi, A. Richter, and V. Koivunen, "Detection and tracking of MIMO propagation path parameters using state-space approach," *IEEE Transactions on Signal Processing*, vol. 57, no. 4, pp. 1538–1550, April 2009.

[30] D. Marquardt, "An algorithm for least-squares estimation of nonlinear parameters," *SIAM J. Appl. Math.*, vol. 11, pp. 431–441, 1963.

Jussi Salmi (S'05–M'09) was born in Finland in 1981. He received his M. Sc. and D. Sc. degrees both with honors from Helsinki University of Technology (HUT), Finland, in 2005 and 2009, respectively. In 2009–2010 he worked as a Postdoctoral Research associate at Dept. of Electrical Engineering, University of Southern California, Los Angeles, CA. Currently he works as a Postdoctoral researcher at Dept. of Signal Processing and Acoustics, Aalto University School of Electrical Engineering (former HUT), Finland. His current research interests include RF-based vital sign detection, UWB MIMO radar, indoor positioning, measurement based MIMO channel modeling, and parameter estimation.

Dr. Salmi is the author of over 30 research papers in international journals and conferences. He has received the Best Student Paper Award in EUSIPCO'06, and co-authored a paper receiving the Best paper Award in Propagation in EuCAP'06.

Andreas F. Molisch (S'89–M95–SM00–F'05) received the Dipl. Ing., Dr. techn., and habilitation degrees from the Technical University Vienna (Austria) in 1990, 1994, and 1999, respectively. From 1991 to 2000, he was with the TU Vienna, becoming an associate professor there in 1999. From 2000-2002, he was with the Wireless Systems Research Department at AT&T (Bell) Laboratories Research in Middletown, NJ, USA. From 2002-2008, he was with Mitsubishi Electric Research Labs, Cambridge, MA, USA, most recently as Distinguished Member of Technical Staff and Chief Wireless Standards Architect. Concurrently he was also Professor and Chairholder for radio systems at Lund University, Sweden. Since 2009, he is Professor of Electrical Engineering at the University of Southern California, Los Angeles, CA, USA, where he heads the Wireless Devices and Systems (WiDeS) group.

Dr. Molisch has done research in the areas of SAW filters, radiative transfer in atomic vapors, atomic line filters, smart antennas, and wideband systems. His current research interests are measurement and modeling of mobile radio channels, UWB, cooperative communications, and MIMO systems. Dr. Molisch has authored, co-authored or edited four books (among them the textbook "Wireless Communications, Wiley-IEEE Press), eleven book chapters, some 130 journal papers, and numerous conference contributions, as well as more than 70 patents and 60 standards contributions.

Dr. Molisch is Area Editor for Antennas and Propagation of the IEEE Trans. Wireless Comm. and co-editor of special issues of several journals. He has been General Chair, TPC Chair, or Track/Symposium Chair of numerous international conferences. He was chairman of the COST 273 working group on MIMO channels, the IEEE 802.15.4a channel model standardization group, Commission C (signals and systems) of URSI (International Union of Radio Scientists, 2005-2008), and the Radio Communications Committee of the IEEE Communications Society (2009-2010). He has received numerous awards, most recently the James Evans Avant-Garde Award of the IEEE VT Society and the Donald Fink Award of the IEEE. Dr. Molisch is a Fellow of the IEEE, Fellow of the IET, and an IEEE Distinguished Lecturer.